CELL BIOLOGY

ROS transfer at peroxisome-mitochondria contact regulates mitochondrial redox

Laura F. DiGiovanni[1,2], Prabhsimran K. Khroud[1,2], Ruth E. Carmichael[3], Tina A. Schrader[3], Shivneet K. Gill[2,4], Kyla Germain[1,2], Robert Y. Jomphe[1,2], Christoph Wiesinger[5], Maxime Boutry[1], Maki Kamoshita[3,6], Daniel Snider[1], Garret Stubbings[7], Rong Hua[1], Noel Garber[1,2], Christian Hacker[3], Andrew D. Rutenberg[7], Roman A. Melnyk[2,4], Johannes Berger[5], Michael Schrader[3], Brian Raught[8,9], Peter K. Kim[1,2,10]*

Maintenance of mitochondrial redox homeostasis is of fundamental importance to cellular health. Mitochondria harbor a host of intrinsic antioxidant defenses, but the contribution of extrinsic, nonmitochondrial antioxidant mechanisms is less well understood. We found a direct role for peroxisomes in maintaining mitochondrial redox homeostasis through contact-mediated reactive oxygen species (ROS) transfer. We found that ACBD5 and PTPIP51 form a contact between peroxisomes and mitochondria. The percentage of these contacts increased during mitochondrial oxidative stress and helped to maintain mitochondrial health through the transfer of mitochondrial ROS to the peroxisome lumen. Our findings reveal a multiorganelle layer of mitochondrial antioxidant defense—suggesting a direct mechanism by which peroxisomes contribute to mitochondrial health—and broaden the scope of known membrane contact site functions.

The formation of reactive oxygen species (ROS) in mitochondria by the electron transport chain (ETC) is a by-product of oxidative metabolism (*1*). Maintenance of mitochondrial redox homeostasis is thought to be a compartmentalized process in which mitochondrial antioxidant systems scavenge ETC-derived ROS (*2*). However, longstanding evidence also indicates that defects in peroxisomes can lead to ROS-mediated mitochondrial damage (*3*, *4*). Peroxisomes are ubiquitous membrane-bound organelles that harbor high concentrations of antioxidant enzymes, particularly catalase (*5*). The peroxisome redox environment is reducing compared with other intracellular environments (*6*–*8*). Mitochondrial oxidative stress is a well-characterized hallmark of peroxisome biogenesis disorders (*3*, *4*), and mitochondria dysfunction is linked to loss of catalase expression, activity, and peroxisomal localization (*7*, *9*, *10*). These findings implicate peroxisomes in the maintenance of mitochondrial redox homeostasis, but the mechanism of this maintenance is not known. Given the antioxidant capacity of peroxisomes, we postulated that they act directly on mitochondrial redox homeostasis as sinks for mitochondrial ROS.

Mitochondria form membrane contact sites with nearly every compartment in the cell (*11*). Such contact sites are essential for maintaining mitochondrial metabolic function, lipid composition, fission, and positioning by facilitating interorganelle transfer of molecules such as lipids, metabolites, and ions (*12*). ROS are known to be signaling molecules for the regulation of mitochondria–endoplasmic reticulum (ER) contact sites (*13*–*17*). However, whether membrane contact sites can also serve to transfer ROS between organelles as an antioxidant function is unclear. We investigated whether a peroxisome-mitochondria (PO-Mito) contact site functions in mitochondrial redox homeostasis by facilitating the transfer of mitochondria-produced ROS to peroxisomes.

Mitochondrial oxidative stress triggers PO-Mito contact

We developed a spatiotemporal imaging method to measure PO-Mito contact. We collected time-lapse multi-*z* images of cells transfected with fluorescent peroxisome and mitochondria markers using high-resolution laser-scanning confocal microscopy and tracked the edge-to-edge pixel distance of each peroxisome to the nearest mitochondria over time (Fig. 1A and fig. S1A). Plotting these apposition events (≤1 pixel) against the duration of association fit a two-component exponential decay model, indicating that two types of peroxisome-mitochondria apposition events with distinct temporal signatures existed (Fig. 1B). Reasoning that apposition events that persist over time were likely true contact events, whereas short events were likely nonspecific interactions or a product of diffraction-limited imaging, we used the slow τ calculated from the two-component exponential decay model to empirically define PO-Mito contact as an apposition event of ≤1 pixel for >31 s. No correlation between this measurement and the volume of mitochondria (fig. S1B) or peroxisomes (fig. S1C) was observed, suggesting that organelle density did not confound measurement. To validate this method of contact quantification, we measured peroxisome-ER contact in COS-7 cells. As expected, decreased peroxisome-ER contact was observed after small interfering RNA (siRNA) depletion of the peroxisome-ER tethers ACBD5 [acyl–coenzyme A (CoA)–binding domain–containing protein 5], VAPA (vesicle-associated membrane protein–associated protein A), and VAPB (fig. S2, A to D) (*18*, *19*). We also observed a robust increase in PO-Mito contact in response to the expression of a PO-Mito artificial tether (AT), a TOM20-Cer-PEX26 fusion protein (fig. S2, E to H).

We next assessed using this metric whether PO-Mito contact responded to mitochondrial oxidative stress. PO-Mito contact in Huh7 cells increased after treatment with rotenone, a potent inducer of mitochondrial ROS (Fig. 1C) (*20*). Similar results were observed when cultured cells were grown in galactose or palmitic acid as more physiological methods to induce mitochondrial ROS production (Fig. 1D and fig. S3, A and B) (*21*, *22*). The observed increase in PO-Mito contact in response to galactose was further validated with a proximity-ligation assay (fig. S3, C and D). Increased PO-Mito contact in galactose- or palmitic acid–supplemented media was attenuated by bolstering mitochondrial redox capacity through expression of catalase targeted to the mitochondria matrix (mt-CAT) in which the peroxisome targeting sequence was deleted (Fig. 1D and figs. S3B and S4). Thus, PO-Mito contact increased in response to elevated mitochondrial oxidative stress.

ACBD5 and PTPIP51 mediate peroxisome-mitochondria contact

Although contact between peroxisomes and mitochondria has been previously observed in mammalian cells, the tethering components have not been identified despite several being described in yeast (*11*, *23*–*25*). To identify and characterize the PO-Mito tethers responsible for this stress-responsive contact, we performed a BioID screen on the peroxisomal tether protein ACBD5, which has been reported to act as a peroxisome-ER tether (Fig. 1E and data S1) (*18*, *19*). The outer mitochondrial membrane protein PTPIP51 (protein tyrosine phosphatase–interacting protein 51), which has been reported to act as a mitochondria-ER tether (*26*), was identified as a potential ACBD5 interacting partner (Fig. 1E and fig. S5). This observation was supported by the reciprocal identification of ACBD5 in a PTPIP51 BioID (fig. S6).

[1]Cell and Systems Biology Program, Hospital for Sick Children, Peter Gilgan Centre for Research and Learning, Toronto, Canada. [2]Department of Biochemistry, University of Toronto, Toronto, Canada. [3]Biosciences, University of Exeter, Exeter, UK. [4]Molecular Medicine Program, Hospital for Sick Children, Peter Gilgan Centre for Research and Learning, Toronto, Canada. [5]Department of Pathobiology of the Nervous System, Center for Brain Research, Medical University of Vienna, Vienna, Austria. [6]Research Institute for Microbial Diseases, Osaka University, Osaka, Japan. [7]Department of Physics and Atmospheric Science, Dalhousie University, Halifax, Canada. [8]Princess Margaret Cancer Centre, University Health Network, Toronto, Canada. [9]Department of Medical Biophysics, University of Toronto, Toronto, Canada. [10]College of Korean Medicine, Kyung Hee University, Seoul, Republic of Korea.
*Corresponding author. Email: pkim@sickkids.ca

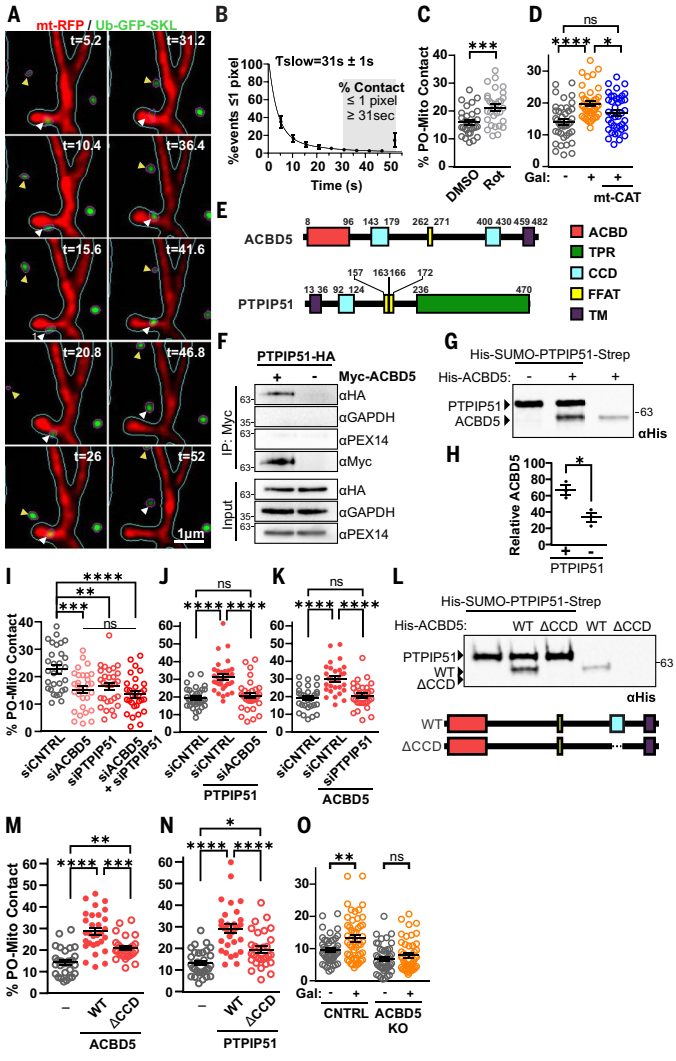

Fig. 1. ACBD5 and PTPIP51 mediate PO-Mito contact in response to mitochondrial oxidative stress. (**A**) Live-cell images of HeLa cells expressing mt-RFP and Ub-GFP-SKL after image segmentation. Blue outline, mitochondria segment; magenta outline, peroxisome segment; white arrow, long apposition; yellow arrow, short apposition; t, time in seconds. (**B**) Percentage of apposition events one pixel or less against duration fit to a two-component exponential decay model ($n = 82$; $N = 9$). (**C** and **D**) Percent PO-Mito contact in Huh7 CNTRL cells treated with 500 nM rotenone (Rot) for 30 min ($n = 30$; $N = 3$) (C) or 4.5 g/liter galactose (+) or glucose (−) ± mt–myc-CAT-ΔKANL (mt-CAT) for 24 hours ($n = 40$; $N = 4$) (D). DMSO, dimethyl sulfoxide. (**E**) Schematics of ACBD5 and PTPIP51. Amino acid positions are indicated. ACBD, acetyl-CoA binding domain; FFAT, two phenylalanines in an acidic tract; CCD, coiled-coil domain; TM, transmembrane; TPR, tetratricopeptide repeat. (**F**) Coimmunoprecipitation (IP) of myc-ACBD5 and PTPIP51–HA (hemagglutinin) in human embryonic kidney–293 cells after formaldehyde cross-linking. (**G** and **H**) Immunoblot (G) and quantification (H) of ACBD5-PTPIP51 binding in vitro. His-SUMO-PTPIP51-Strep was immobilized on magnetic beads by a strep tag and incubated with His-ACBD5, both from bacteria lysate. (**I** to **K**) Percent PO-Mito contact in HeLa cells with ACBD5 and/or PTPIP51 siRNA ($n = 30$; $N = 3$) (I) ± expression of PTPIP51-HA ($n = 32$; $N = 3$) (J) or myc-ACBD5 ($n = 30$; $N = 3$) (K). (**L**) Immunoblot of in vitro binding of PTPIP5 to ACBD5WT (WT) or ACBD5ΔCCD (ΔCCD) as in (G). (**M** and **N**) Percent PO-Mito contact in HeLa cells overexpressing exogenous WT or ΔCCD Myc-ACBD5 (M) or PTPIP51-HA ($n = 30$; $N = 3$) (N). (**O**) Percent PO-Mito contact in CNTRL or ACBD5KO Huh7 cells cultured in glucose or galactose [$n = 50$, 50, 47, and 49 (left to right); $N = 5$]. *n*, number of cells; *N*, independent experiments; two-tailed Mann-Whitney test (C); one-way analysis of variance (ANOVA) with post hoc Tukey's test [(D), (I) to (K), (M), and (N)]; two-tailed unpaired *t* test (H); two-way ANOVA with post hoc Tukey's test (O). Data are mean ± SE. $^*P < 0.05$; $^{**}P < 0.01$; $^{***}P < 0.001$; $^{****}P < 0.0001$; ns, not significant.

Exogenously expressed ACBD5 and PTPIP51 could be coimmunoprecipitated (Fig. 1F), and direct interaction between these proteins was corroborated by use of a bacterial expression system (Fig. 1, G and H). PO-Mito contact decreased in HeLa cells after siRNA-mediated depletion of ACBD5 or PTPIP51, with no additive decrease observed upon co-depletion (Fig. 1I and fig. S7A). Conversely, overexpression of ACBD5 or PTPIP51 resulted in increased PO-Mito contact, which was prevented by siRNA depletion of the counterpart (Fig. 1, J and K). Increased PO-Mito contact after ACBD5 and PTPIP51 overexpression was also observed with electron microscopy (fig. S7, B to D). A direct ACBD5-PTPIP51 interaction thus appeared to regulate PO-Mito contact.

AlphaFold multimer simulations (fig. S8) of ACBD5 and PTPIP51 in both a 1:1 heterodimer (fig. S8, C and D) and 2:2 hetero-tetramer (fig. S8, E and F) yielded high-confidence positioning between coiled-coil domains (CCDs), which were predicted as antiparallel left-handed coiled coils (fig. S8G). Consistent with this prediction, a CCD deletion mutant of ACBD5 (ACBD5ΔCCD) (fig. S9A) did not interact with PTPIP51 in vitro (Fig. 1L and fig. S9, B and C), even when in far excess of wild-type (WT) ACBD5 (fig. S9, D and E). Furthermore, ACBD5ΔCCD and a CCD deletion mutant of PTPIP51 (PTPIP51ΔCCD) (fig. S9F) displayed an impaired ability to increase PO-Mito contact in HeLa cells compared with the full-length proteins (Fig. 1, M and N). The CCDs thus appeared to be required to mediate ACBD5-PTPIP51 interaction and were critical for the formation of PO-Mito contact.

A Huh7 cell line in which ACBD5 was deleted (ACBD5KO) displayed reduced PO-Mito contact that was rescued by the reintroduction of ACBD5 but not ACBD5ΔCCD (fig. S10, A to D). ACBD5KO cells did not have impaired peroxisomal density or matrix protein import but rather displayed enhanced localization of peroxisome matrix proteins catalase and ACOX1 (fig. S10, E to H). ACBD5KO cells displayed a slight decrease in peroxisomal β-oxidation of C16:0 dicarboxylic fatty acid (16-DCA) (fig. S10I), which is consistent with previous reports for C26:0 (*27*–*29*). No difference was observed in the acetate:carbon dioxide (CO_2) ratio after pulse-chase with 16-DCA (fig. S10, I to K), indicating that transport of peroxisome-derived β-oxidation intermediates to the mitochondria was not impaired. The degradation of palmitic acid also had no defect (fig. S10L), indicating that mitochondrial β-oxidation was not impaired. However, in contrast to control (CNTRL) cells, PO-Mito contact did not increase in ACBD5KO Huh7 cells when galactose was the primary carbon source (Fig. 1O and fig. S3, C and D), indicating that contact mediated by ACBD5-PTPIP51 was up-regulated in response to elevated mitochondrial oxidative metabolism.

Peroxisome contact maintains mitochondrial redox homeostasis

Reversible conversion between reduced glutathione (GSH) and oxidized glutathione (GSSG) is a central cellular antioxidant system to catalyze reduction of hydrogen peroxide (H_2O_2). Steady-state GSSG:GSH is often used as a metric of compartmental redox state. The cytoplasmic glutathione pool of ACBD5KO cells was more oxidative than CNTRL cells, as determined by cytoplasmic Grx1-roGFP2 (c-Grx1-roGFP2) (Fig. 2, A and B), a ratio-metric reporter for the GSSG:GSH ratio that detects endogenous changes in subcellular redox (*14*, *30*). ACBD5KO cells also had elevated nuclear levels of nuclear factor erythroid 2–related factor 2 (NRF2), a transcription factor that responds to oxidative stress by inducing the expression of antioxidant response genes. NRF2 nuclear localization was indicated with a size shift previously shown to represent nuclear NRF2 and that mimicked the response seen with H_2O_2 treatment (Fig. 2, C and D, and fig. S11, A and B) (*31*). These data indicated a generally elevated cellular oxidative state in cells deficient in PO-Mito contact.

Mitochondria fusion is activated upon mitochondrial oxidative stress (*32*, *33*). We therefore assessed whether mitochondrial morphology was altered in ACBD5KO cells as an indicator of mitochondrial oxidative stress in cells deficient in PO-Mito contact. Mitochondria in ACBD5KO

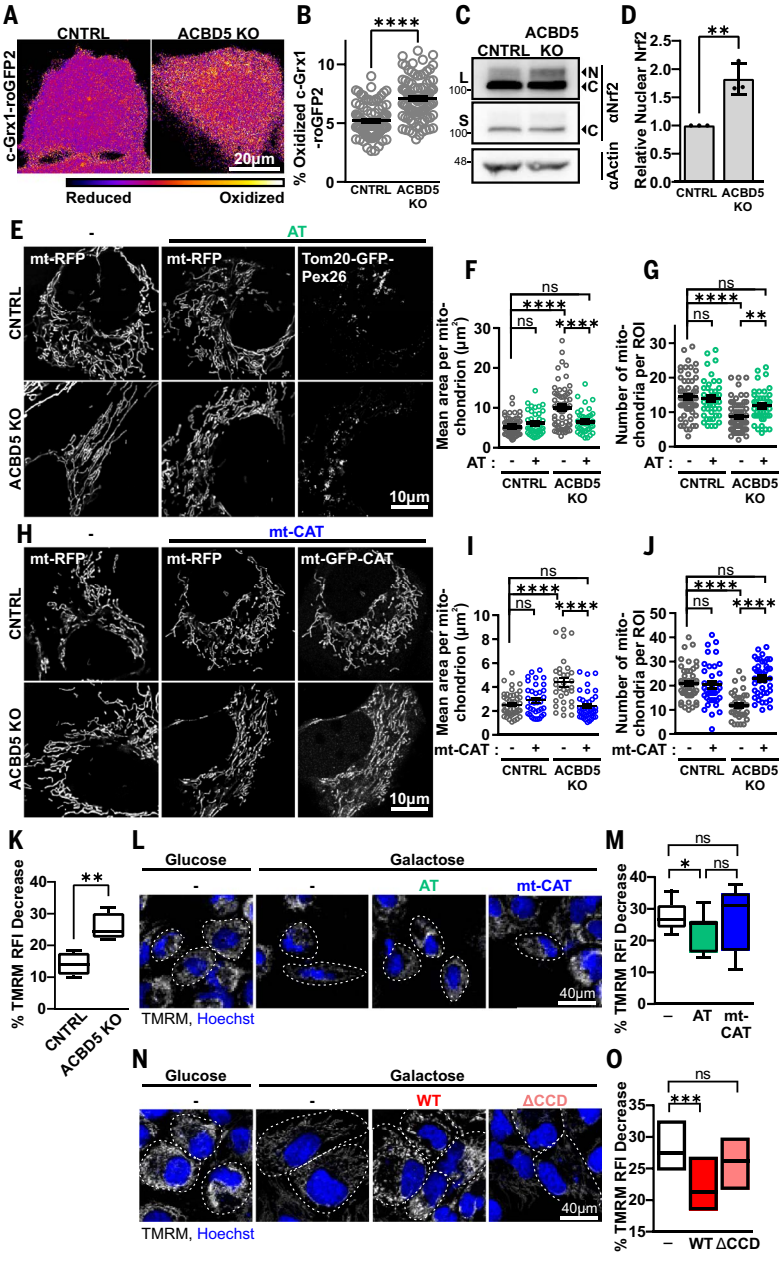

Fig. 2. Peroxisome contact maintains mitochondrial redox homeostasis. (**A**) Representative images of c–Grx1-roGFP2 in CNTRL and ACBD5KO Huh7 cells. Spectrum scale represents the 400:480 emission ratio. (**B**) Percent oxidation quantified from (A) [$n = 96$ and 91 (left to right); $N = 6$]. (**C** and **D**) Immunoblot (C) and quantification (D) of nuclear Nrf2 in CNTRL and ACBD5KO Huh7 cells. C, cytoplasmic; L, long exposure; N, nuclear; S, short exposure. (**E**) Representative images of mitochondria in CNTRL and ACBD5KO Huh7 cells ± expression of TOM20-GFP-PEX26 (AT). (**F** and **G**) Mean area per mitochondrion (F) and mitochondrial number per region of interest (ROI) (G) quantified from (E) [$n =$ 61, 42, 64, and 44 (left to right); $N = 5$]. (**H** to **J**) As (E) to (H) with expression of mt–GFP-CAT-ΔKANL (mt-CAT) [$n =$ 46, 36, 37, and 41 (left to right); $N = 3$]. (**K**) Percent decrease in average TMRM intensity after galactose treatment quantified from fig. S11, F and G ($N = 4$). RFI, relative fluorescence intensity. (**L** and **N**) Representative images of TMRM in ACBD5KO Huh7 cells transfected with H2B-GFP alone or coexpressed with AT or mt–myc-CAT-ΔKANL (mt-CAT) (L) or H2B-GFP alone or coexpressed with WT or ΔCCD Myc-ACBD5, cultured in 4.5 g/liter glucose or galactose media for 24 hours (N). Dashed outline, transfected cells. (**M** and **O**) Percent decrease in average TMRM intensity after galactose treatment quantified from (L) ($N = 7$) (M) or from (N) ($N = 3$) (O). *n*, number of cells; *N*, independent experiments; two-tailed Mann-Whitney test (B); two-tailed unpaired *t* test [(D) and (K)]; two-way ANOVA with post hoc Tukey's test [(F), (G), (I), and (J)]; repeated measures one-way ANOVA with post hoc Tukey's test [(M) and (O)]. Data are mean ± SE [(B), (D), (F), (G), (I), and (J)]; Box plots show quartiles with whiskers to 5th and 95th percentile [(K), (M), and (O)].

cells displayed an elongated morphology in comparison with CNTRL cells, as measured by an increase in mitochondrial area and a decrease in mitochondrial number (Fig. 2, E to J). We observed no difference in mitochondria density between CNTRL and ACBD5KO cells, indicating that mitochondrial biogenesis was not affected (fig. S11C). Mitochondria morphology in ACBD5KO cells was rescued by restoring PO-Mito contact through expression of the PO-Mito AT (Fig. 2, E to G), indicating that the elongated morphology was due to loss of PO-Mito contact. Similarly, morphology was also rescued by expression of mt-CAT (Fig. 2, H to J, and fig. S4), suggesting that elongated mitochondrial morphology in ACBD5KO cells was due to elevated mitochondrial oxidative stress.

Mild membrane decoupling is used by mitochondria as an antioxidant mechanism (*34*). We therefore examined mitochondrial membrane potential in ACBD5KO cells using tetramethylrhodamine methyl ester (TMRM) under nonquenching conditions (fig. S11, D and E) as an indicator of elevated mitochondrial oxidative stress. ACBD5KO cells displayed a significant reduction in mitochondria membrane potential compared with that of CNTRL cells under basal growth conditions (fig. S11, F and G). ACBD5KO cells also displayed a significantly greater loss in mitochondria membrane potential in response to galactose compared with that of CNTRL cells (Fig. 2K and fig. S11, F and G). The galactose-induced decrease in mitochondrial membrane potential in ACBD5KO cells was mitigated by the expression of the PO-Mito AT (Fig. 2, L and M) and ACBD5WT but not ACBD5ΔCCD (Fig. 2, N and O). This indicated that ACBD5-mediated PO-Mito contact was protective against ROS-induced loss of mitochondria membrane potential. A significant rescue was not observed after mt-CAT expression (Fig. 2, L and M), which is consistent with previous reports that showed defects in membrane potential after overexpression of mitochondrially targeted antioxidants, potentially because of impaired redox regulation of mitochondrial function (*35*). Thus, markers of mitochondrial oxidative stress were elevated in ACBD5KO Huh7 cells that were deficient in PO-Mito contact.

PO-Mito contact mitigates mitochondrial oxidative stress

We observed no difference in basal mitochondria glutathione redox state between CNTRL and ACBD5KO Huh7 cells using mitochondria matrix–targeted Grx1-roGFP2 (mt-Grx1-roGFP2) (Fig. 3, A to C, and fig. S12, A and B). This was potentially due to the compensatory adaptive changes to mitigate oxidative stress described above or because PO-Mito contact may only contribute to redox homeostasis under conditions of oxidative stress. We therefore assessed the ability of ACBD5KO cells to maintain mitochondrial redox homeostasis using a combination of oxidative stresses and redox probes (Fig. 3A). ACBD5KO cells cultured in galactose displayed significantly elevated mitochondrial glutathione oxidation, whereas CNTRL cells showed no significant change (Fig. 3, B and C). Increased mt–Grx1-roGFP2 oxidation in galactose-treated ACBD5KO cells was abolished by expression of the PO-Mito AT (Fig. 3, B to C) and ACBD5WT but not ACBD5ΔCCD (Fig. 3, D and E). Thus, PO-Mito contact contributed to mitigating mitochondrial ROS produced by galactose metabolism,

resulting in increased reliance on glutathione for redox homeostasis in ACBD5KO cells.

Similar results were observed after acute oxidative insult through mitochondrially targeted KillerRed (mt-KR), a fluorophore that induces mitochondrial ROS production in a manner that is linearly dependent on mt-KR expression (*36*). Acute mitochondrial ROS production was induced by photobleaching mt-KR, and the change in mitochondrial glutathione redox state was determined by comparing mt-roGFP2 before and after bleach. The change in mt-roGFP2 as a function of mt-KR expression was larger in ACBD5KO cells than in CNTRL cells (fig. S12, C and D), indicating that ACBD5KO cells depended more on glutathione to scavenge equivalent levels of ROS compared with CNTRL cells. This increase was rescued by coexpression of the PO-Mito AT, confirming that PO-Mito contact contributed to a reduction of mitochondrial-produced ROS.

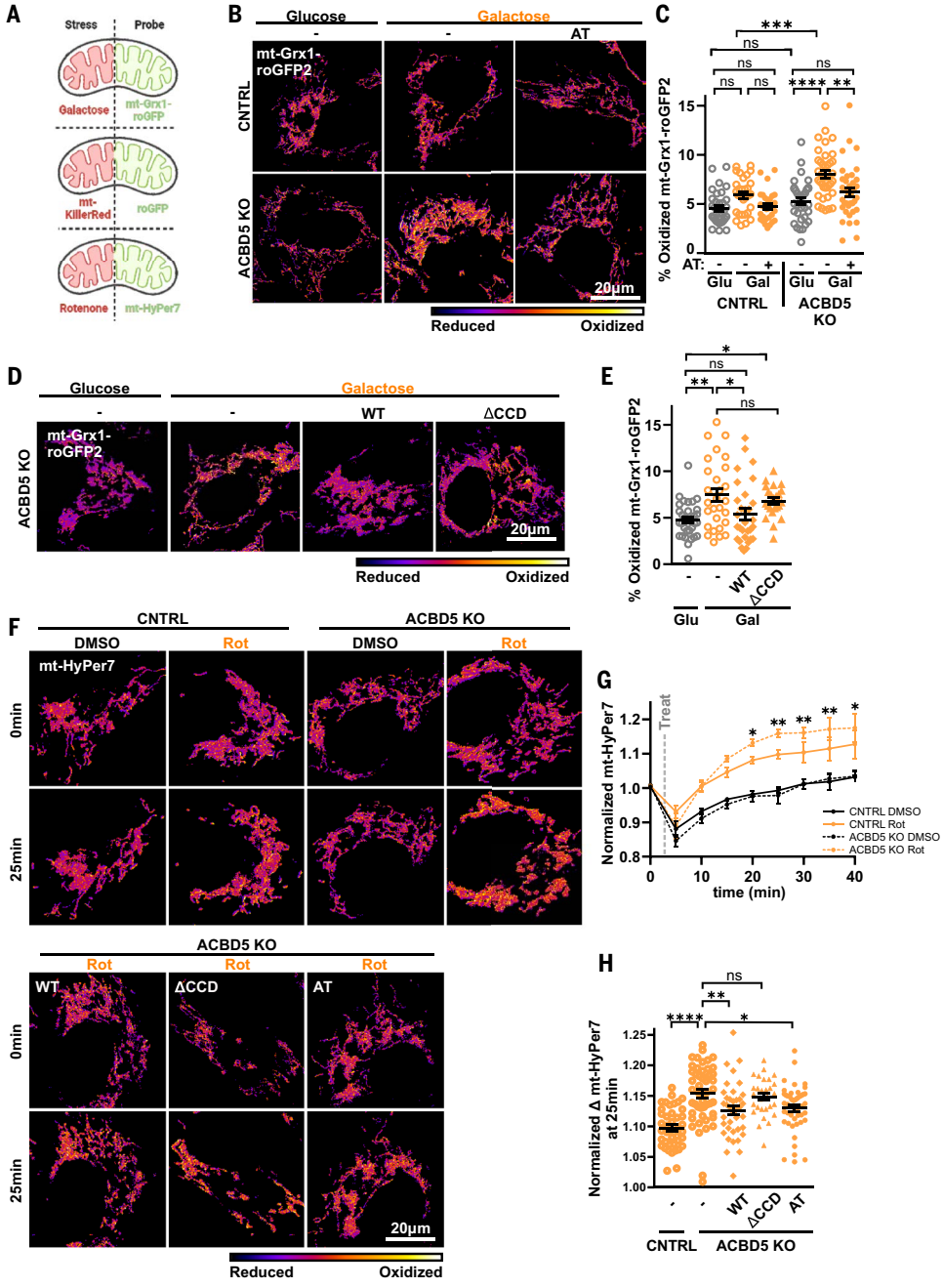

Fig. 3. Peroxisome contact mitigates mitochondrial oxidative stress. (**A**) Schematic of stress and probe experimental conditions. (**B** and **D**) Representative images of CNTRL and ACBD5KO Huh7 cells transfected with mt–Grx1-roGFP2 and AT (B) and ACBD5KO Huh7 cells transfected with mt–Grx1-roGFP2 and WT or ΔCCD Myc-ACBD5, cultured for 24 hours in 4.5 g/liter glucose (Glu) or galactose (Gal) (D). Spectrum scale represents the 400:480 ratio of emitted fluorescence. (**C** and **E**) Percent oxidation of mt–Grx1-roGFP2 quantified from (B) [$n = 33, 32, 31, 34, 38$, and 37 (left to right); $N = 3$] (C) or quantified from (D) [$n = 33, 29, 32$, and 27 (left to right); $N = 3$] (E). (**F**) Representative images of mt-HyPer7 expressed in CNTRL and ACBD5KO Huh7 cells with and without cotransfection with AT, Myc-ACBD5WT, or Myc-ACBD5ΔCCD as indicated, before or 25 min after addition of 20 nM rotenone (Rot). (**G**) Quantification of change in average mt-HyPer7 ratio over 40 min after rotenone or vehicle treatment ($N = 4$). (**H**) Quantification of change in mt-HyPer7 ratio per cell after 25 min of rotenone treatment ($n = 41, 49, 38, 29$, and 47; $N = 4$). Data are mean ± SE. *n*, number of cells analyzed; *N*, independent experiments; two-way ANOVA with post hoc Tukey's test [(C) and (G)]; one-way ANOVA with post hoc Tukey's test [(E) and (H)].

We also used HyPer7 (*37*) targeted to the mitochondria matrix (mt-HyPer7) to directly measure mitochondrial H_2O_2 after induction of mitochondrial ROS production with rotenone. The mt-HyPer7 oxidation increased over 40 min after rotenone treatment to a greater extent in ACBD5KO Huh7 cells than in CNTRL cells (Fig. 3, F and G). We also observed this enhanced rotenone-induced stress in A549 cells depleted of ACBD5 by means of siRNA (fig. S12, E and F). The effect of rotenone on mt-HyPer7 in ACBD5KO cells was attenuated by expression of the PO-Mito AT and ACBD5WT but not ACBD5ΔCCD (Fig. 3, F and H). This indicated that the ability of mitochondria to mitigate rotenone-induced H_2O_2 was dependent on ACBD5-mediated contact. Thus, ACBD5-mediated PO-Mito contact was a critical mechanism for maintaining mitochondrial redox homeostasis during oxidative stress.

Contact facilitates transfer of mitochondrial ROS to peroxisomes

We hypothesized that PO-Mito contact facilitated transfer of mitochondrial-produced ROS to peroxisomes to mitigate mitochondrial oxidative stress. In support of this model, catalase localization to the peroxisome was strongly enhanced in cells cultured in galactose-supplemented media (fig. S13, A to D) despite no change in total catalase abundance (fig. S13, E and F). Catalase localization to peroxisomes was also enhanced after treatment with rotenone and became even more apparent when cells were first cultured in galactose (fig. S13, G and H), which is in line with the dependence of rotenone-induced ROS formation on NADH:NAD^+ (reduced nicotinamide adenine dinucleotide:oxidized nicotinamide adenine dinucleotide). This increased peroxisomal redox capacity in response to mitochondrial oxidative stress was consistent with peroxisomes acting as reducing sinks for mitochondrial ROS. The stress-induced catalase phenotype in CNTRL cells was also similar to the enhanced peroxisomal localization of catalase seen basally in ACBD5KO cells (fig. S10, E, G, and H), suggesting that ACBD5KO cells experienced higher oxidative stress under basal conditions, in line with our previous observations.

To directly test the role of peroxisomes as reducing sinks for mitochondrially produced ROS, we measured peroxisomal redox status in response to mitochondrial oxidative stress induction (Fig. 4A). Using Grx1-roGFP2 targeted to the peroxisome matrix (Grx1-roGFP2-SKL) (fig. S14, A and B), we found that peroxisomal glutathione oxidation increased after galactose-induced mitochondrial oxidative stress in CNTRL Huh7 cells (Fig. 4, B and C). This increase could be attenuated by the expression of mt-CAT, confirming that the galactose-induced changes in peroxisome redox state were directly linked to ROS production in the mitochondria. Unfortunately, peroxisome matrix–targeted HyPer7 (fig. S14, C and D) was unsuitable for assessing peroxisomal H_2O_2 in response to mitochondrial oxidative stress because the change in catalase localization upon rotenone treatment (fig. S13, G and H) had a confounding influence on direct measurement of H_2O_2 by HyPer7 (fig. S15).

To test whether transfer of mitochondrial ROS to peroxisomes occurred through PO-Mito contact, we assessed whether the responsiveness of peroxisomal redox status to mitochondrial oxidative stress was impaired in ACBD5KO cells. Although basal peroxisomal glutathione oxidation was elevated in ACBD5KO cells compared with CNTRL, no change was observed upon expression of either the PO-Mito AT (fig. S16, A and B) or mt-CAT (fig. S16, C and D), indicating this increase was unrelated to both PO-Mito contact and mitochondrial redox. This elevated baseline glutathione oxidation in ACBD5KO cell peroxisomes could have been due to elevated ACOX1, previously described in ACBD5KO mice (*29*) and observed by us in this work (fig. S10G), or the elevated cytosolic glutathione oxidation observed in ACBD5KO cells (Fig. 2, A and B) leading to impaired cytosolic reduction of peroxisomal GSSG (*38*).

The galactose-induced increase in peroxisomal glutathione oxidation was significantly lower in ACBD5KO cells than in CNTRL cells (Fig. 4, D and E, and fig. S16E),

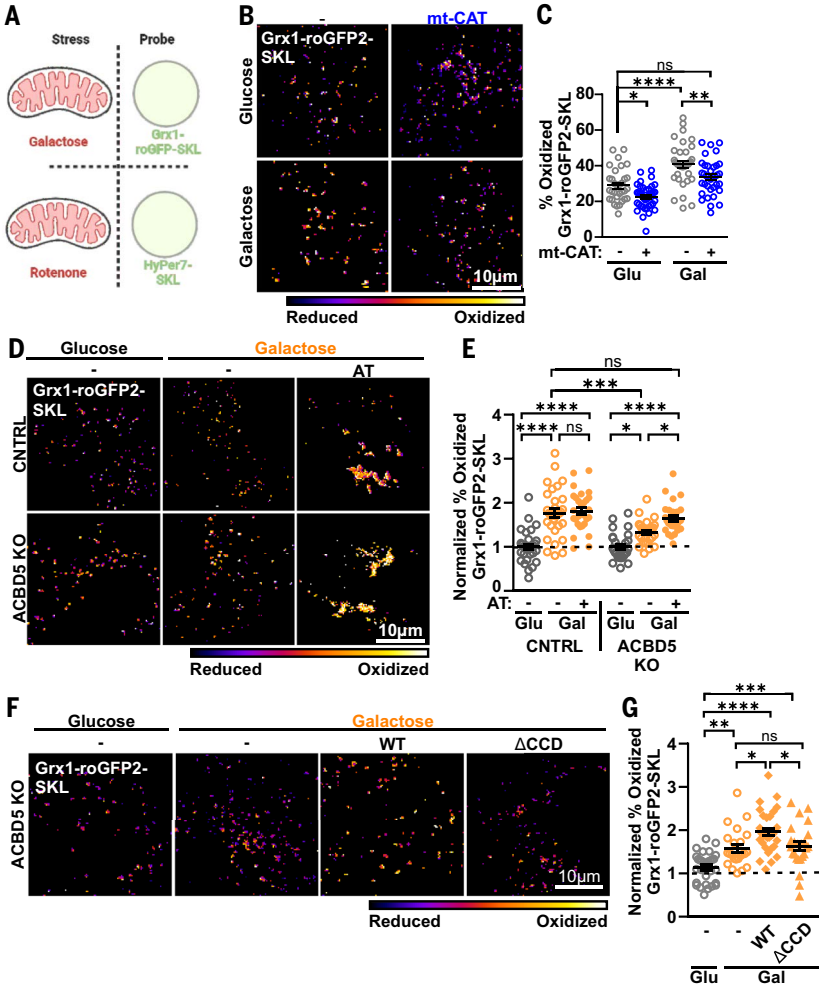

Fig. 4. Mitochondrial-produced ROS are transferred to peroxisomes at contact sites. (**A**) Schematic of stress and probe experimental conditions. (**B**) Representative images of CNTRL Huh7 cells transfected with Grx1-roGFP2-SKL and cultured in 4.5 g/liter glucose (Glu) or galactose (Gal) for 24 hours, with and without coexpression of mt–myc-CAT-ΔKANL (mt-CAT). The spectrum scale represents the 400:480 ratio of emitted fluorescence. (**C**) Percent oxidation of Grx1-roGFP2-SKL quantified from (A) [n = 32, 40, 37, and 36 (left to right); N = 4]. (**D** and **F**) Representative images of CNTRL and ACBD5KO Huh7 cells transfected with mGrx1-roGFP2-SKL and AT (D) and ACBD5KO Huh7 cells transfected with Grx1-roGFP2-SKL with and without cotransfection with Myc-ACBD5WT or Myc-ACBD5ΔCCD (F), cultured for 24 hours in 4.5 g/liter glucose, galactose, or galactose. Spectrum scale represents the 400:480 ratio of emitted fluorescence. (**E** and **G**) Percent oxidation of Grx1-roGFP2-SKL quantified from (D) [n = 33, 31, 28, 29, 29, and 27 (left to right); N = 3] (E) or quantified from (F) [n = 43, 38, 41, and 35 (left to right); N = 3] (G), normalized to glucose-treated condition within each cell type. n, number of cells analyzed; N, independent experiments; two-way ANOVA with post hoc Tukey's test [(C) and (E)]; one-way ANOVA with post hoc Tukey's test (G). Data are mean ± SE.

indicating that transfer of mitochondrial ROS to peroxisomes was impaired in cells that were deficient in PO-Mito contact. The response of peroxisomal redox state to galactose in ACBD5KO cells could be rescued with expression of the PO-Mito AT (Fig. 4, D and E, and fig. S16E) and ACBD5WT but not ACBD5ΔCCD (Fig. 4, F and G, and fig. S16F). Thus, the transfer of mitochondrial ROS to peroxisomes occurred through a mechanism dependent on PO-Mito contact.

Discussion

Although a correlation between peroxisome dysfunction and mitochondrial oxidative stress is well established, no mechanistic link has been identified. Our study demonstrated a direct role for peroxisomes in maintaining mitochondrial redox homeostasis through contact-mediated ROS transfer. We identified a PO-Mito contact site mediated by peroxisomal membrane protein ACBD5 and outer mitochondrial membrane protein PTPIP51. We demonstrated that this contact, as well as peroxisomal redox capacity, was dynamically regulated in response to mitochondrial oxidative stress to facilitate ROS transfer and maintain mitochondrial redox homeostasis (fig. S17). This study uncovered a direct functional role for peroxisomes in the maintenance of mitochondrial redox homeostasis and revealed that mitochondrial stress in peroxisomal diseases could be due to loss of contact-mediated transfer of mitochondrial ROS to peroxisomes. We described evidence of ROS exchange between organelle lumens and matrices as an antioxidant mechanism, transforming our understanding of how cells respond to oxidative stress and indicating that redox homeostasis is a multiorganelle process.

Efflux of mitochondrial ROS to peroxisomes is a conceptually attractive mechanism to prevent mitochondrial oxidative damage. Because mitochondria contain large amounts of iron, the transfer of ROS to peroxisomes would prevent hydroxyl radical formation and oxidative damage of mitochondria. Additionally, because NADPH (reduced nicotinamide adenine dinucleotide phosphate) is not consumed during the reduction of H_2O_2 by catalase, peroxisome reduction of mitochondrial ROS is not directly affected by limitations imposed by NADPH regeneration, unlike the glutathione system.

Our work showed that contact sites mediate the transfer of ROS between organelle lumens and matrices. We postulate that ROS trafficking between organelles may be more prevalent than previously assumed and that peroxisomes may also regulate redox homeostasis of other organelles, such as phagosomes (*39*) and the ER (*40*, *41*).

To explain how peroxisome contact could robustly act to transfer ROS produced across the mitochondrial network, we postulate that sites of peroxisome contact are spatially coupled to ETC activity and ROS production. Spatial specificity is relevant to other mitochondrial contacts; for example, ER-mitochondria contacts are juxtaposed to mitochondrial contact site and cristae organizing system (MICOS) complexes, and PO-Mito contacts in yeast are adjacent to sites of mitochondrial acetyl-CoA synthesis (*42*, *43*). Although metabolic subdomains within mitochondria have not been well documented, studies have shown that individual cristae have distinct membrane potentials and are functionally independent, indicating that ROS production in mitochondria could be spatially regulated (*44*).

REFERENCES AND NOTES

1. M. P. Murphy, *Biochem. J.* **417**, 1–13 (2009).
2. A. O. Oyewole, M. A. Birch-Machin, *FASEB J.* **29**, 4766–4771 (2015).
3. E. Baumgart *et al.*, *Am. J. Pathol.* **159**, 1477–1494 (2001).
4. R. S. Rahim, M. Chen, C. C. Nourse, A. C. B. Meedeniya, D. I. Crane, *Neuroscience* **334**, 201–213 (2016).
5. P. E. Purdue, P. B. Lazarow, *J. Cell Biol.* **134**, 849–862 (1996).
6. M. Schrader, H. D. Fahimi, *Biochim. Biophys. Acta* **1763**, 1755–1766 (2006).
7. O. Ivashchenko *et al.*, *Mol. Biol. Cell* **22**, 1440–1451 (2011).
8. T. Yano *et al.*, *Mol. Cell. Biol.* **30**, 3758–3766 (2010).
9. P. A. Walton, M. Pizzitelli, *Front. Physiol.* **3**, 108 (2012).
10. J. I. Koepke *et al.*, *Traffic* **8**, 1590–1600 (2007).
11. A. M. Valm *et al.*, *Nature* **546**, 162–167 (2017).
12. C. S. Harper, A. J. White, L. L. Lackner, *Curr. Opin. Cell Biol.* **65**, 58–65 (2020).
13. D. M. Booth, B. Enyedi, M. Geiszt, P. Várnai, G. Hajnóczky, *Mol. Cell* **63**, 240–248 (2016).
14. D. M. Booth, P. Várnai, S. K. Joseph, G. Hajnóczky, *Mol. Cell* **81**, 3866–3876.e2 (2021).
15. M. Beretta *et al.*, *EMBO J.* **39**, e103530 (2020).
16. A. Bassot *et al.*, *Cell Rep.* **42**, 111899 (2023).
17. X. Zhang *et al.*, *EMBO J.* **38**, e100871 (2019).
18. R. Hua *et al.*, *J. Cell Biol.* **216**, 367–377 (2017).
19. J. L. Costello *et al.*, *J. Cell Biol.* **216**, 331–342 (2017).
20. J. F. Turrens, A. Boveris, *Biochem. J.* **191**, 421–427 (1980).
21. C. Aguer *et al.*, *PLOS ONE* **6**, e28536 (2011).
22. R. A. Egnatchik, A. K. Leamy, Y. Noguchi, M. Shiota, J. D. Young, *Metabolism* **63**, 283–295 (2014).
23. L. Hicks, H. D. Fahimi, *Cell Tissue Res.* **175**, 467–481 (1977).
24. M. Mattiazzi Ušaj *et al.*, *J. Mol. Biol.* **427**, 2072–2087 (2015).
25. N. Shai *et al.*, *Nat. Commun.* **9**, 1761 (2018).
26. K. J. De Vos *et al.*, *Hum. Mol. Genet.* **21**, 1299–1311 (2012).
27. Y. Yagita *et al.*, *J. Biol. Chem.* **292**, 691–705 (2017).
28. S. Ferdinandusse *et al.*, *J. Med. Genet.* **54**, 330–337 (2017).
29. W. Darwisch *et al.*, *Commun. Biol.* **3**, 713 (2020).
30. M. Gutscher *et al.*, *Nat. Methods* **5**, 553–559 (2008).
31. T. Shinjo *et al.*, *PLOS ONE* **13**, e0196191 (2018).
32. T. Shutt, M. Geoffrion, R. Milne, H. M. McBride, *EMBO Rep.* **13**, 909–915 (2012).
33. S. Mattie, J. Riemer, J. G. Wideman, H. M. McBride, *J. Cell Biol.* **217**, 507–515 (2018).
34. S. Cadenas, *Biochim. Biophys. Acta Bioenerg.* **1859**, 940–950 (2018).
35. D. E. Handy *et al.*, *J. Biol. Chem.* **284**, 11913–11921 (2009).
36. M. E. Bulina *et al.*, *Nat. Biotechnol.* **24**, 95–99 (2006).
37. V. V. Pak *et al.*, *Cell Metab.* **31**, 642–653.e6 (2020).
38. M. J. Ferreira *et al.*, *Redox Biol.* **63**, 102764 (2023).
39. F. Di Cara, A. Sheshachalam, N. E. Braverman, R. A. Rachubinski, A. J. Simmonds, *Immunity* **47**, 93–106.e7 (2017).
40. W. J. Kovacs *et al.*, *J. Biol. Chem.* **284**, 7232–7245 (2009).
41. Y. Liu *et al.*, *Cell Death Differ.* **16**, 847–857 (2009).
42. P. S. Tirrell, K. N. Nguyen, K. Luby-Phelps, J. R. Friedman, *J. Cell Biol.* **219**, e202003024 (2020).
43. Y. Cohen *et al.*, *Mol. Biosyst.* **10**, 1742–1748 (2014).
44. D. M. Wolf *et al.*, *EMBO J.* **38**, e101056 (2019).
45. D. Snider, J. Sing, ceryltan, H. D'Souza, Single_Cell_Analysis_Toolkit: Release v1. Zenodo (2025); https://doi.org/10.5281/zenodo.15287825.
46. G. Stubbings, Peroxisome-Mitochondria-Fitting: Public release of peroxisome mitochondria fitting code. Zenodo (2025); https://doi.org/10.5281/zenodo.15304836.

ACKNOWLEDGMENTS

We thank J. Brumell for the critical reading of the manuscript. The model was created with BioRender.com. **Funding:** This work was suppported by the Canadian Institutes of Health Research (PJT 180476 to P.K.Ki and B.R.); the Natural Sciences and Engineering Research Council of Canada (RGPIN-2020-05865 to P.K.Ki. and RGPIN-2019-05888 to A.D.R.); the Austrian Science Fund (FWF P31082 to C.W. and FWF P34723 to J.B.); the Biotechnology and Biological Sciences Research Council (BB/T002255/1 and BB/W015420/1 to M.S., BB/V018167/1 to M.S. and R.E.C., and BB/Z514767/1 to R.E.C.); the Canadian Institutes of Health Research Doctoral Research Award (FRN 164257 to L.F.D.); a RESTRACOMP award from the Hospital for Sick Children (to L.F.D.); a RESTRACOMP award from the Hospital for Sick Children (to R.Y.J.); a Canadian Institutes of Health Research Fellowship Award (to M.B.); a RESTRACOMP fellowship from the Hospital for Sick Children (to M.B.); a John Evans Leadership Fund grant from the Canadian Foundation for Innovation (to P.K.Ki.); and the Ontario Innovation Trust (to P.K.Ki.). **Author contributions:** Conceptualization: L.F.D., P.K.Ki. Formal Analysis: L.F.D., P.K.Kh., M.K., C.H., K.G., R.Y.J., M.B., C.W., R.E.C., T.A.S. Methodology: L.F.D., P.K.Ki. Investigation: L.F.D., P.K.Kh., M.K., C.H., K.G., R.Y.J., C.W., S.K.G., R.E.C., T.S., R.H. Visualization: L.F.D., N.G. Funding acquisition: P.K.Ki., A.D.R., J.B., M.S., B.R., L.F.D., M.B., R.E.C. Project administration: L.F.D., P.K.Ki., A.D.R., J.B., M.S., B.R., R.A.M. Software: D.S. , G.S. Supervision: P.K.Ki. Writing – original draft: L.F.D., P.K.Ki. Writing – review and editing: L.F.D., P.K.Ki., M.B., C.W., J.B., M.S., B.R., R.E.C. **Competing interests:** L.F.D. is also affiliated with Pre-Amp. K.G. is also affiliated with Denali Therapeutics. M.B. is also affiliated with the Institut de Génétique et de Biologie Moléculaire et Cellulaire. All other authors declare no competing financial interests. **Data and materials availability:** All data needed to evaluate our conclusions are in the main paper or the supplementary materials. Cell lines used in this study are available on request. All mass spectroscopy data have been deposited at https://massive.ucsd.edu (accession: MSV000093219). Codes to perform 3D image segmentation and organelle tracking (*45*) and to fit apposition duration histograms to a two-component exponential decay (*46*) are available.

SUPPLEMENTARY MATERIALS

science.org/doi/10.1126/science.adn2804
Materials and Methods; Figs. S1 to S19; Table S1; References (*47*–*64*); MDAR Reproducibility Checklist; Data S1

Submitted 3 December 2023; resubmitted 11 February 2025; accepted 8 May 2025

10.1126/science.adn2804